Available online at www.sciencedirect.com
ScienceDirect
Acta Materialia 58 (2010) 1837–1849
Acta MATERIALIA
www.elsevier.com/locate/actamat

Characterizing short-range vs. long-range spatial correlations in dislocation distributions

Juliette Chevy [a,b,*], Claude Fressengeas [c], Mikhail Lebyodkin [c], Vincent Taupin [c], Pierre Bastie [d,e], Paul Duval [a]

[a] Laboratoire de Glaciologie et Géophysique de l'Environnement—CNRS, 54 rue Molière, 38402 St. Martin d'Hères, France
[b] Laboratoire Science et Ingénierie des Matériaux et Procédés, Grenoble INP-CNRS-UJF, BP 75, 38402 St. Martin d'Hères Cedex, France
[c] Laboratoire de Physique et Mécanique des Matériaux, Université Paul Verlaine—Metz/CNRS, Ile du Saulcy, 57045 Metz Cedex, France
[d] Laboratoire de Spectrométrie Physique, BP 87, 38402 St. Martin d'Hères Cedex, France
[e] Institut Laue Langevin, BP 156, 38042 Grenoble Cedex 9, France

Received 24 July 2009; received in revised form 16 November 2009; accepted 20 November 2009
Available online 21 December 2009

Abstract

Hard X-ray diffraction experiments have provided evidence of a strongly heterogeneous distribution of dislocation densities along the axis of cylindrical ice single crystals oriented for basal slip in torsion creep. The dislocation arrangements showed a complex scale-invariant character, which was analyzed by means of statistical and multifractal techniques. A trend to decreasing autocorrelation of the dislocation distribution was observed as deformation proceeds. At low strain levels, long-range spatial correlations control the distribution, but short-range correlations in relation with cross-slip progressively prevail when strain increases. This trend was reproduced by a model based on field dislocation dynamics, a theory accounting for both long-range elastic interactions and short-range interactions through transport of dislocation densities.

Keywords: Dislocation dynamics; Self-organization; Spatial correlation; Hard X-ray diffraction

1. Introduction

Dislocation-mediated plasticity is commonly considered as a regular process occurring smoothly in time and homogeneously in space, as suggested by the term "plastic flow" used to describe this plasticity. Conventional wisdom contends that fluctuations of dislocation activity are sufficiently small and independent of one another to add at random, over sufficiently large length and time scales, to a net smooth and homogeneous overall response. However, recent studies have offered evidence that, instead, plasticity is a scale-invariant phenomenon characterized by power law distributions of avalanche size, and by space and time coupling over several orders of magnitude [1–7]. In all of these studies, the long-range lattice distortion and internal stress field associated with the presence of dislocations are considered to be involved in the self-organization of the plastic activity. Dislocation distributions reflect in space the history and properties of the past plastic activity. Hence, characterizing post-mortem dislocation patterns yields information about the dynamic processes that led to these arrangements. In X-ray-transparent solids such as ice, bulk characterization of dislocation dynamics processes is therefore feasible via X-ray diffraction techniques. Earlier work in that field [8] reported scale-invariance of the axial dislocation distribution in ice single crystals deformed in torsion creep at moderate strain, with long-range spatial correlations also attributed to the lattice

* Corresponding author. Address. Laboratoire de Glaciologie et Geophysique de l'Environnement—CNRS, Mechanical Science and Engineering Department, 1206 W. Green Street—158 MEB, Urbana, IL 61801-2906, United States.
E-mail address: juliette.chevy@gmail.com (J. Chevy).

1359-6454/$36.00 © 2009 Acta Materialia Inc. Published by Elsevier Ltd. All rights reserved.
doi:10.1016/j.actamat.2009.11.027

distortion and elastic internal stress fields. In contrast, unstrained samples showed no evidence of spatial correlation. From these results, one may erroneously infer that more strain and larger dislocation densities lead to enhanced long-distance correlations. It is shown in the following that such is not the case.

In the present paper, we report on ice single crystals deformed in torsion creep at moderate to large strains. We use the hard X-ray diffraction technique as a model approach to investigate the self-organization of dislocation distributions. We believe that such experiments are insightful in the context of dislocation self-organization for several reasons. First, torsion tests involve stress and strain gradients from the axis to the edge of the sample, and therefore their accommodation by "geometrically necessary" or "polar" dislocations, whose densities are associated with lattice distortion and internal stress fields. Using single crystals avoids introducing additional complexity due to dislocation–grain boundary interactions. Under terrestrial temperature and pressure conditions, ice has a hexagonal crystallographic structure. It is a particularly suitable material for the present purpose due to its strong anisotropy of slip. Indeed, ice deforms almost exclusively by glide of dislocations in the basal planes [9]. In particular, the torsion of single crystals whose crystallographic c-axis is oriented along the torsion axis is accommodated by $\langle 1\,1\,\bar{2}\,0\rangle$ screw dislocations, which leads to the emergence of strong elastic internal stresses [10,11]. Unlike the applied stress field, the internal stress field has non-basal components. Therefore it favors the transport of dislocations along the c-axis by the occurrence of double cross-slip of screw dislocations through prismatic planes [10,12]. Hence, there is the distinct possibility that the short-range interactions inherent to double cross-slip could also be involved in the self-organization of the plastic activity, complementing long-range stresses. Indeed, double cross-slip tends to disseminate slip activity along the c-axis, while the edge jogs formed in the prismatic planes during the process may serve as strong obstacles to dislocation motion. Such a distinct role of short-range correlations is likely to be effective at large strains, when dissemination of slip by cross-slip becomes significant. Note that the role of short-range correlations was suggested in recent work on dislocation patterning [13] and on the intermittency of plastic activity [10,14–16]. Therefore, the objectives of the present paper are threefold: (i) to show that characterizing the role of short-range vs. long-range correlations in the self-organization of dislocation ensembles is possible from the experimental analysis of the spatial distribution of dislocation densities; (ii) to show the progressive prevalence of short-range over long-range correlations in dislocation self-organization as strain increases; and (iii) to retrieve the above trends in the dislocation distributions predicted by a heuristic field dislocation dynamics model featuring internal stresses and dislocation transport.

The outline of the paper is therefore as follows. Section 2 deals with the experimental procedure used to provide dislocation distributions through torsion tests and hard X-ray diffraction analysis. The tests are performed at different strain levels to follow the evolution of spatial correlations with strain. A statistical analysis and a multifractal analysis are used to accurately monitor possible variations in the correlation regime. The results and their multifractal analysis are presented in Section 3. Although the reader is referred to Ref. [17] for a general presentation of the method, the section offers a short primer on the multifractal techniques of data analysis. Section 4 is devoted to an interpretation of the results based on a field dislocation dynamics theory that accounts for both long-range correlations through internal stress field development, and short-range correlations through dislocation transport [18]. Here, the aim is to provide evidence that such generic features lead to behavior similar to our experimental results in a simple representative situation. A summary and conclusions complete the paper.

2. Experimental procedure

2.1. Torsion tests

Laboratory-grown single crystals were used for the torsion experiments. The initial dislocation density of these crystals, measured by hard X-ray diffraction analysis (see below) was less than 10^8 m^{-2}. The orientation of the samples was chosen to align the torsion axis with the c-axis. Basal planes were therefore parallel to the permanent shear plane, within an accuracy of $\pm 1^\circ$. A constant torsion torque was applied to all samples, leading to ice deformation by creep, while no load was applied in the axial direction. The temperature of the cold room was maintained at -15 °C, the diameter and height of all samples were both 43 mm. The applied torque, 2.14 N m, corresponded to an applied stress of 0.12 MPa at the edge of the sample. Note that a characteristic elastic shear modulus of ice is $\mu = 3$ GPa. Defining the torsion strain as $\gamma = R\theta/h$, where θ is the torsion angle, h the height and R the radius of the samples, three samples were respectively strained at 0.6%, 5% and 56%. The macroscopic homogeneity of strain along the torsion axis was controlled by monitoring a marker line drawn along the sample, parallel to the axis. Fig. 1 shows the strain vs. time curve obtained for the most deformed sample.

2.2. Dislocation density distributions

In order to obtain dislocation density distributions from lattice distortion characterization, X-ray synchrotron topography (XRST) analysis was used in Ref. [8], but since the technique is limited to low dislocation densities, hence to low strains <3%, hard X-ray diffraction was also employed at a larger strain (namely 4.35%). In the present work, radial slices 1 mm thick, of height $\Delta x < h$, were extracted from the samples after deformation for hard X-ray diffraction analysis. The experiments were carried out

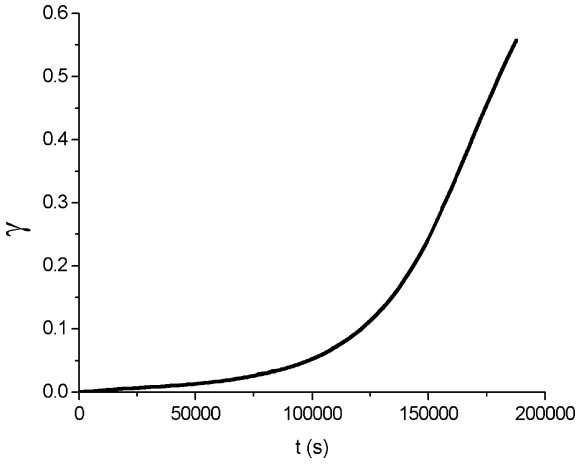

Fig. 1. Creep curve (strain vs. time) for an ice single crystal deformed in torsion at −15 °C. The diameter and height of the sample are both 43 mm. A 2.14 N m torque is applied, corresponding to an applied stress of 0.12 MPa at the edge of the sample. Maximum strain is $\gamma = 56\%$. Note the unremitting acceleration of creep except, perhaps, at the largest strains.

at the Institut Laue Langevin in Grenoble, using an industrial high-voltage X-ray tube (420 kV) and the original Laue hard X-ray technique, which allows bulk observation of samples more than 1 cm thick. The energy range of the white divergent beam was between 100 and 400 keV, corresponding to wavelengths between 0.003 and 0.012 nm. This technique is based on a focusing effect occurring when a divergent X-ray beam diffracts through the crystal [19] (see Fig. 2). All X-rays diffracted by planes belonging to the same crystallographic family converge along a single line on a focal surface, on points symmetrical about the source point with respect to the normal to the diffracting planes. Owing to high energies, the Bragg angles are small (about 1°) and the focal surface can thus be approximated by a plane. Further, all the diffraction lines obtained from the different families of planes are located close to the transmitted beam in the same focal plane. The detector, composed of an X-ray intensifier and a CCD camera, is set in the focal plane perpendicular to the direct beam to record the resulting Laue diagram. A schematic Laue diagram obtained from the prismatic planes of one of our samples is shown in Fig. 3, along with information useful for the analysis. A point in the diagram has components (θ, x) where θ is the torsion angle introduced in Section 2, and x represents the location along the c-axis. As we show below, the slope of the diffracted lines in the diagram is directly related to the axial lattice distortion and to a "geometrically necessary" or "polar" dislocation density. In contrast with the so-called "statistical" dislocations, the latter are dislocations arranged in an orderly fashion, which effectively result in lattice distortion. Both notions will be extensively surveyed in Section 4.

On account of the crystal orientation in the torsion test, the distortion of the prismatic planes is the most significant for our purposes. The corresponding diffraction line extends in both the x and θ directions of the diagram. In the θ direction, $\Delta\theta$ denotes the difference in angular distortion over the distance Δx, between the prismatic planes on top and to the bottom of the analyzed slice. At a local point (θ, x) along the diffraction line, $\delta\theta$ is the increment in distortion between two consecutive measurement points located at a distance δx along the c-axis. Concurrently, $\delta\theta$ and $\Delta\theta$ are also the corresponding increments in the Bragg angle. Hence, Bragg angle and torsion angle variations are identical. Any dislocation lying in the crystal slice between two consecutive measurement points is unresolved, and the slice must therefore be considered as undistorted for all practical matters. An overall survey of the diffraction line shows that it is rectilinear at a sufficiently large scale of observation. This is an indication that the macroscopic strain is homogeneously distributed along the sample axis. The (roughly linear) relationship between δx and $\delta\theta$ that could be extracted from this overall dependence has a very poor resolution (0.35 mm/pixel). Instead, we prefer using the fluctuations in the local diffracted intensity, which give a much better resolution. Indeed, according to the kinematic theory of diffraction, the diffracted intensity is proportional to the diffracting volume. Thus, knowing from the measurements the local and total diffracted intensity δI_θ at point (x, θ) and $I_{tot} = \sum \delta I_\theta$, δx can be written as

$$\delta x = \Delta x \frac{\delta I_\theta}{I_{tot}} \tag{1}$$

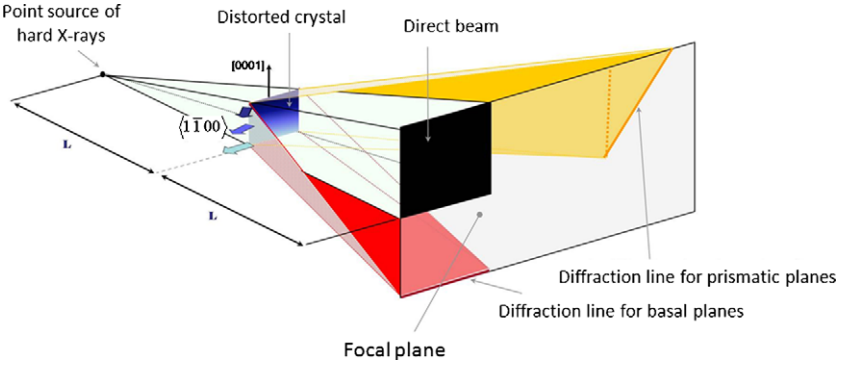

Fig. 2. Hard X-ray diffraction method. The divergent beam diffracts through a slice extracted from a sample distorted by torsion about the c-axis. The Laue diagram, comprising the transmitted beam and the lines diffracted by the basal and the prismatic planes, is seen in the focal plane.

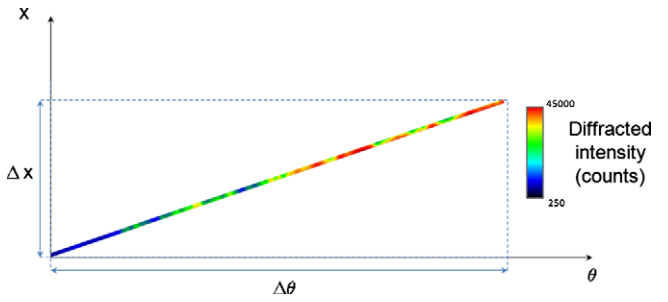

Fig. 3. A Laue diagram showing the line diffracted by the prismatic planes in a slice extracted from a sample distorted by torsion about the c-axis. The color code quantifies the diffracted intensity along the line. Δx represents the height of the slice, $\Delta\theta$ denotes both the Bragg angle and torsion angle variation along the slice.

The axial lattice distortion is $\delta\theta/\delta x$, and a volumetric polar dislocation density can be defined as the ratio

$$\rho = \frac{1}{b}\frac{\delta\theta}{\delta x} \tag{2}$$

where b is the length of the Burgers vector [20]. Comprehensive justification for this relation will be provided in Section 4 below. Using Eq. (2), the knowledge of $(\delta\theta, \delta x)$ arising from the interpretation of the Laue diagram allows the profile of the dislocation density ρ to be plotted along the c-axis. If the above macroscopic linear fitting is used, Eq. (2) leads to the mean volumetric dislocation density $\bar{\rho}$. Instead, a fairly good resolution can be obtained if relation (1) is employed. Note that for a given angular resolution $\Delta\theta_0$ of the experimental set up ($\delta\theta \geqslant \Delta\theta_0$, with $\Delta\theta_0 = 0.17'$), the number of measurement points available is $N = \Delta\theta/\Delta\theta_0$. Therefore, the mean spatial resolution $\langle\delta x\rangle = \Delta x/N$ improves as $\Delta\theta$ increases, and hence when strain increases (see Table 1). For sample 3 $\langle\delta x\rangle = 1.7$ μm compares with the resolution obtained from XRST.

Undesirable effects such as a residual background noise due to beam diffusion and a systematic increase in the diffracted intensity δI_θ with the square of the Bragg angle [21,22] were present in earlier work using hard X-ray diffraction [8], which may well have biased the analysis of correlations. Such spurious effects were removed from the present Laue diagrams. In practice, as the diagrams cover only about 1° of torsion angle, several diagrams obtained by rotating the sample around the c-axis are needed to deal with the range of distortion over the height Δx of the slice. The complete dislocation distribution is obtained by patching together the distributions obtained from all these diagrams. The procedure was carried out for samples 1–3, as shown in Figs. 4–6. All the characteristics of the analyzed slices are presented in Table 1.

Table 1
Characteristics of the samples analyzed by hard X-ray diffraction.

Sample	Height (mm)	Local distortion (deg/mm)	Mean spatial resolution (mm)
1	24	1.45×10^{-2}	1.75×10^{-1}
2	16	1.6×10^{-1}	1.8×10^{-2}
3	18	1.63	1.7×10^{-3}

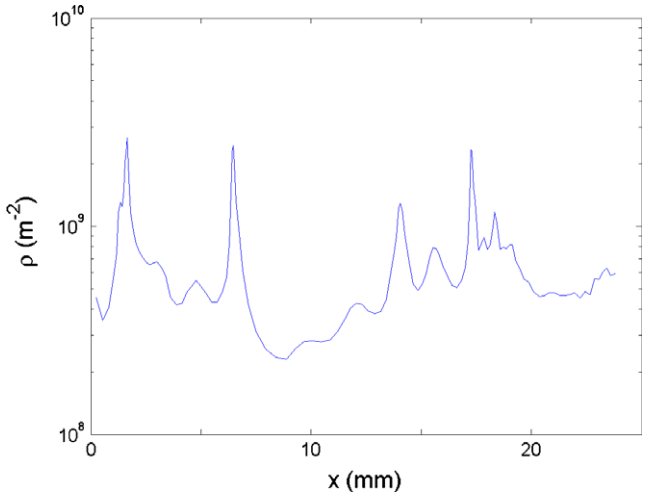

Fig. 4. Dislocation density distribution along the sample axis; sample 1, low strain $\gamma = 0.6\%$.

3. Results

Figs. 4–6 show the distribution of the dislocation density along the sample axis in samples 1–3. The figures reveal the heterogeneous nature of the distribution and its increasing complexity as deformation proceeds. With δ_ρ the standard deviation, the fluctuations of the dislocation density about a mean value $\bar{\rho}$ are roughly characterized by the relative standard deviation $\delta_\rho/\bar{\rho}$. A value close to zero of the latter suggests a rather uniform distribution with limited fluctuations, as in the case of the less deformed sample (see Table 2). A value much larger than 1, as obtained for the most deformed sample, however, indicates a large dispersion of the fluctuation size and some difficulties in defining an

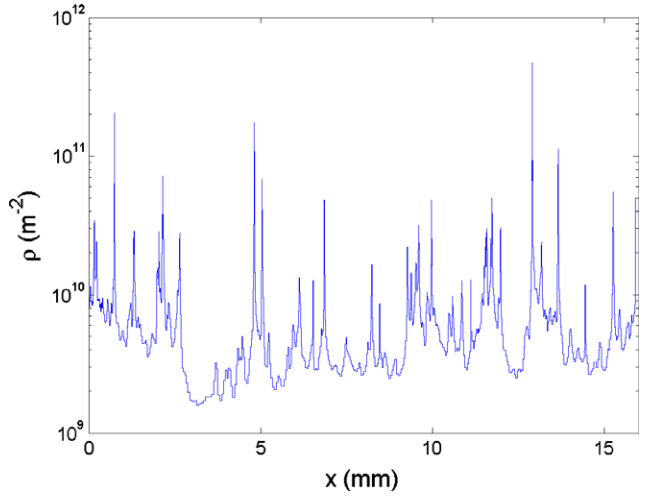

Fig. 5. Dislocation density distribution along the sample axis; sample 2, medium strain $\gamma = 5\%$.

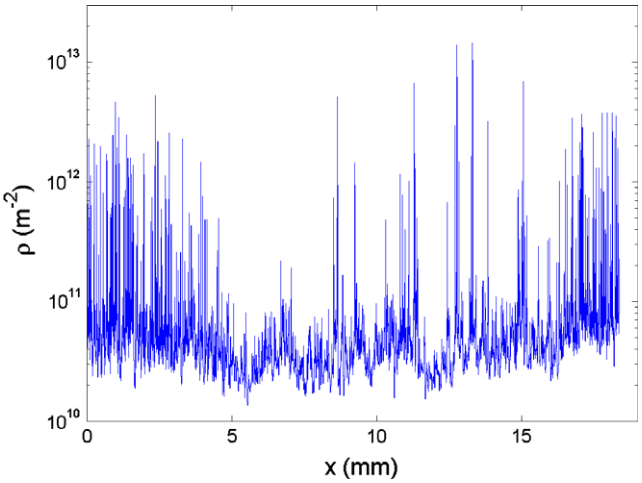

Fig. 6. Dislocation density distribution along the sample axis; sample 3, large strain $\gamma = 56\%$.

Table 2
Characteristics of the samples analyzed by hard X-ray diffraction.

Sample	Strain (%)	$\delta_\rho/\bar{\rho}$	$\bar{\rho}$ (m^{-2})
1	0.6	6.41×10^{-1}	10^9
2	5	2.46	10^{10}
3	56	3.80	10^{11}

average value at all. Note that the mean dislocation density value $\bar{\rho}$ strongly increases with strain. A second approach in analyzing more closely the complexity of the dislocation distribution consists in computing the autocorrelation function $r(k)$

$$r(k) = \frac{1}{N-k} \frac{\sum_{n=1}^{N-k} (\rho_n - \bar{\rho})(\rho_{n+k} - \bar{\rho})}{\frac{1}{N}\sum_{n=1}^{N} (\rho_n - \bar{\rho})^2} \quad (3)$$

Here k is an index for the interval between two measurement sites. It represents intervals ranging from the resolution length scale to half the length of the sample. The autocorrelation function is plotted in Fig. 7 for the three samples. By simply defining the characteristic autocorrelation distance as the value of k when $r = 0.5$, it is seen that, for the less deformed sample, the dislocation density is spatially correlated over a range of the order of several millimeters along the axis, but that this distance is much shorter in samples 2 and 3. At first glance, this trend to less spatial correlation seems surprising, since the overall values of lattice distortion and dislocation density $\bar{\rho}$ increase with strain. At least, a decreasing autocorrelation distance strongly suggests the notion that an evolution with strain of the underlying regime of dislocation interactions is taking place.

Fast Fourier transformation (FFT) of the autocorrelation function yields the power spectrum of the dislocation distributions. As shown in Fig. 8, the power spectra are characterized by scaling laws $P(f) = f^{-\mu}$ over a fairly large length scale range (typically between 100 μm and several millimeters in sample 1). Such a property indicates scale-invariance of the diffracted intensity, hence of the dislocation density distribution along the torsion axis, over distances of the order of several millimeters in sample 1. In turn, this scale-invariance implies that the dislocation density distribution is spatially correlated on a large scale, which confirms the trend implied by the autocorrelation function. Such large-scale spatial correlations were also reported in Ref. [8]. They are the fingerprint for long-distance interactions between dislocations. However, if scaling exponents μ can be defined for each sample, the overall trend at low frequencies (large length scales) from one sample to the other is to decreasing exponents (in absolute value) as strain increases, which heralds faster decay of spatial correlations. In addition, several scaling regimes seem to hold at large vs. low frequencies (short vs. large length scales), for small vs. large dislocation density fluctuations in samples 2 and 3, in contrast to sample 1. Hence, several

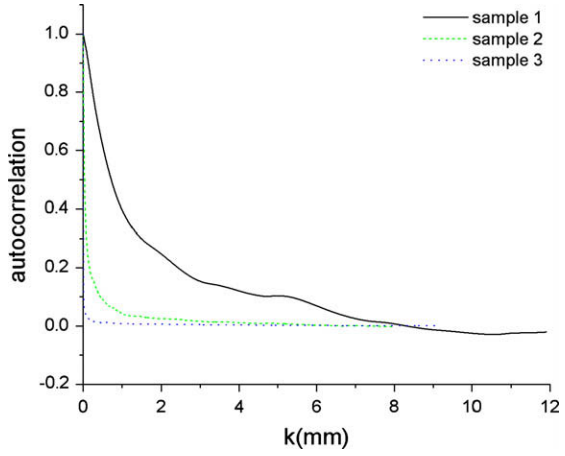

Fig. 7. Autocorrelation function for the three samples: sample 1, black solid line; sample 2, dashed green line; sample 3, dotted blue line. (For interpretation of the references to colour in this figure legend, the reader is referred to the web version of this article.)

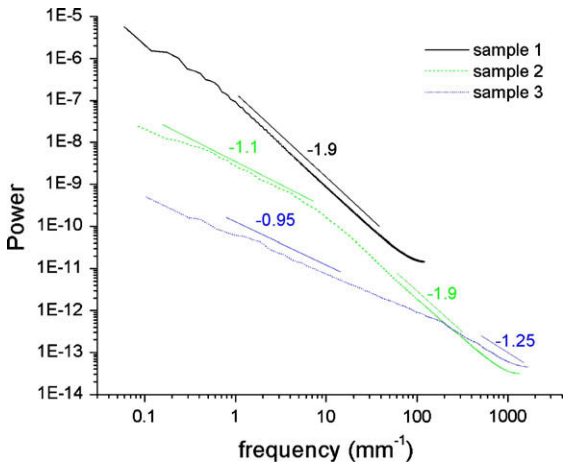

Fig. 8. FFT power spectra for the three samples: sample 1, black solid line; sample 2, dashed green line; sample 3, dotted blue line. (For interpretation of the references to colour in this figure legend, the reader is referred to the web version of this article.)

interaction mechanisms seem to operate simultaneously at different length scales and fluctuation sizes in these two samples, in contrast to sample 1 (and to spectra from Ref. [8]) where a unique correlation regime appears.

The statistical approaches based on the autocorrelation function and the spectral power density are "global" in the sense that all fluctuation sizes and all length scales receive equal treatment. We feel the need for a more accurate statistical description in order to investigate the complexity of the correlation regime. Due to its ability at focusing selectively on different fluctuation sizes, a multifractal analysis seems appropriate in the present situation. The selectivity of the method should yield a more detailed description of scale-invariance, particularly regarding its manifestations on several length scales.

With this aim, the sample axis is subdivided into equal intervals δx (to avoid confusion note that, in contrast, the interval δx was dependent on the diffracted intensity in Eqs. (1) and (2)). A local probability measure $\mu_i(\delta x)$ of the ith interval is defined as the area under the curve $\rho(x)$ within the interval, normalized by the total area calculated over the entire axis. Hence, this measure reflects the distribution of lattice distortion along the axis. The overall sum of μ_i-values equals unity, consistent with the definition of probability. In practice, a proxy for the area is the sum of all $\rho(x)$-magnitudes within the interval. The generalized dimension spectrum, $D(q), q \in \mathbb{Z}$, is computed by constructing the family of partition functions $Z_q(\delta x) = \sum_i \mu_i^q(\delta x)$ for different values of q, where the sum is taken over all space intervals. Therefore, any scale-invariance of the measure μ_i shows up through a power-law $Z_q(\delta x)$ dependence. By definition, the generalized fractal dimension $D(q)$ characterizes scale-invariant behavior when $Z_q(\delta x) \sim \delta x^{(q-1)D(q)}$ as $\delta x \to 0$. In practice, only finite intervals of power-law $Z_q(\delta x)$ dependence are found, due to finite resolution and limited system size. Large values of the measure μ_i dominate in $Z_q(\delta x)$ for large positive q-values, whereas small values correspond to large negative q-values. A varying $D(q)$ reflects scale-invariance characterized by multiple exponents and multi-scale correlations in the underlying physical process, a property referred to as "multifractality". A single value of $D(q) < 1, \forall q$ uncovers a "monofractal", i.e. a simple fractal structure with scale-invariance characterized by a single exponent. "Monofractality" is a much more demanding property than multifractality, because it requires uniformity of scale-invariance over all fluctuation scales. Note that a trivially self-similar stochastic noise leads to the unique value $D(q) = 1, \forall q$.

A complementary point of view is also provided by an equivalent presentation using the singularity spectrum, $(\alpha, f(\alpha))$, related to $D(q)$ via the Legendre transformation [23]. Here, α reflects the local singularity of the measure, $\mu_i(\delta x) \sim \delta x^{\alpha}$, and $f(\alpha)$ represents the fractal dimensions of the subsets of singularities with strength close to α: $N_\alpha(\delta x) \sim \delta x^{-f(\alpha)}$ ($N_\alpha(\delta x)$ denotes the number of intervals in this subset). In the present work, the singularity spectrum was calculated using a direct method [24], which avoids the inaccuracies resulting from the derivatives in the Legendre transform.

Because of a lack of data due to the poor resolution for the less-deformed sample, this analysis will be performed only for samples 2 and 3. We start with the analysis of the dislocation density distribution in the sample loaded at intermediate strain (sample 2, see Fig. 5). From a statistical point of view, there are very few fluctuations in the distribution (about 150), and the analysis is necessarily limited in scope. Nevertheless, multifractality of the distribution can be proved and, hence, the scale-invariance uncovered by the autocorrelation and FFT analysis can be independently confirmed. Indeed, Fig. 9 shows the partition functions on a logarithmic scale for various q-values. Linear variation is seen with varying slope, which is an indication of multifractality (multiple scale-invariance), a property not shown by the autocorrelation and FFT analysis. The range for scale-invariance is short, from $\delta x \sim 0.9$ mm to 4.5 mm. It involves length scales comparable with the sample height $h = 43$ mm. The singularity spectrum (i.e. the variation of $f(\alpha)$ with α) is shown in Fig. 10. The minimum α value is seen to be low (left branch, $\alpha_{min} = 0.18$), and the spectrum therefore suggests that the large fluctuations are very singular, which confirms a visual impression from Fig. 5.

We now focus on the analysis of the dislocation density distribution at high strain shown in Fig. 6. Fig. 11 shows the partition functions in logarithmic scale for various q-values. Again, linear variation is seen with varying slope, which is an indication of multifractality of the distribution. Small (resp. large) values of the slope correspond to large positive (resp. negative) q-values, and to large-scale (resp. small-scale) fluctuations. Straight dashed lines are visual guide for the scaling interval at large fluctuation scale. The latter ranges from $\delta x \sim 0.8$ mm to 12 mm, which cor-

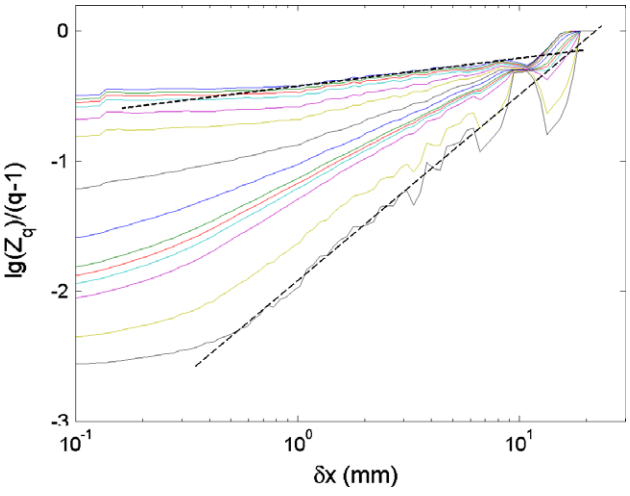

Fig. 9. Partition functions. Sample 2, medium strain $\gamma = 5\%$. q is varied from 20 to -2. The curves for $q < -2$ are not shown to preserve readability, because scatter considerably increases for large negative qs (cf. error bars in Fig. 10). This remark applies to all subsequent figures showing partition functions.

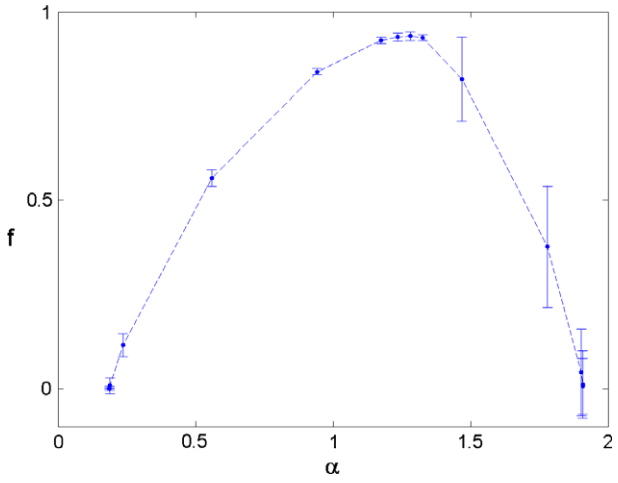

Fig. 10. Singularity spectrum. Sample 2, medium strain $\gamma = 5\%$.

responds to the distance between the largest fluctuations in the distribution. The power law is an excellent fit at positive q-values. The quality of the fit degrades at negative qs. The solid line underlines the scaling regime at small fluctuation scales. It can be seen that the latter extends to small distances $\delta x \sim 0.04$ mm at small q-values, but that it vanishes at large q-values. The corresponding multifractal (i.e. the variation of $D(q)$ with q) and singularity spectra are shown in Figs. 14 and 15.

Since two different scaling regimes for small vs. large fluctuations seem to show up in Fig. 11 (as they independently did in Fig. 8), it is certainly tempting to duplicate the analysis after separating the small fluctuations from the large fluctuations. As there are fluctuations at all scales, the threshold $\delta\rho_c$ between these two species is somewhat arbitrary, but the most representative pattern is obtained for $\delta\rho_c = 5 \times 10^{11}$ m^{-2}. The result for small fluctuations

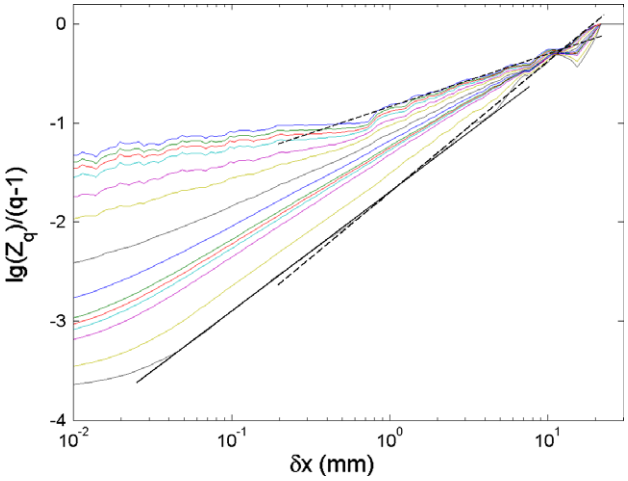

Fig. 11. Sample 3, large strain $\gamma = 56\%$; partition functions, all fluctuations; q is varied here from 20 to −2. Small (resp. large) values of the slope correspond to large positive (resp. negative) q-values, and to large-scale (resp. small-scale) fluctuations. Dashed (resp. solid) lines are visual guides for the scaling interval at large (resp. small) fluctuation scale.

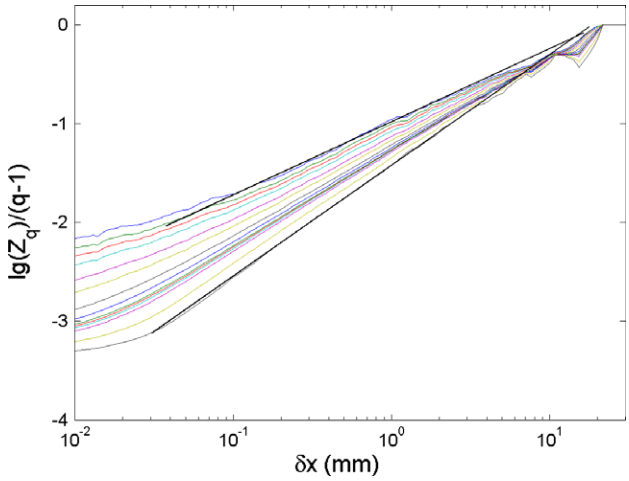

Fig. 12. Sample 3, large strain $\gamma = 56\%$; partition functions, small fluctuations. Straight solid lines are visual guides in the scale-invariant range. The lower line, obtained for low q-values, approximately corresponds to the solid line in Fig. 11.

is shown in Fig. 12. A convincing scaling regime is obtained for all q-values, in the range $\delta x \sim 0.1$–2 mm. The bottom line obtained for low q-values corresponds to the solid line in Fig. 11, and the resulting multifractal and singularity spectra are shown in Figs. 14 and 15 using triangles. The partition functions for the large fluctuations are shown in Fig. 13. Power laws are matched in the range $\delta x \sim 1$–12 mm. As expected for large fluctuations, good quality of the fit is only seen at large positive q-values, and quality is low at negative values. The corresponding multifractal and singularity spectra are also shown in Figs. 14 and 15 with open circles. In these figures, the large-scale and overall scale spectra (resp. open and solid circles) are quite similar, particularly in the most significant range, i.e. at large qs. The singularity index α is smaller for the large fluctuations (the singularity is higher), as one could expect, and

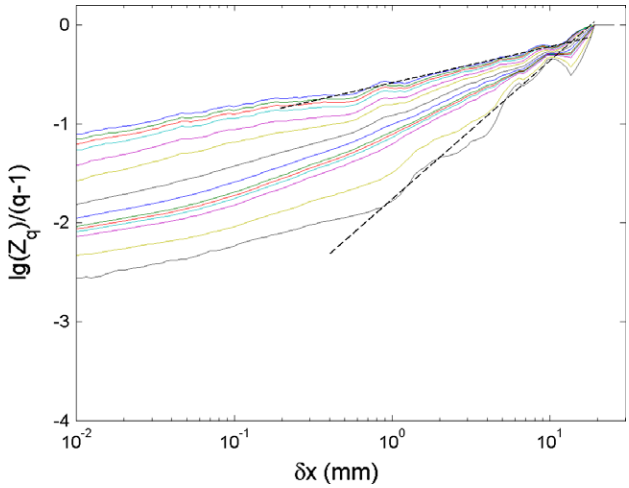

Fig. 13. Sample 3, large strain $\gamma = 56\%$; partition functions, large fluctuations. Straight dashed lines are visual guides in the scale-invariant range.

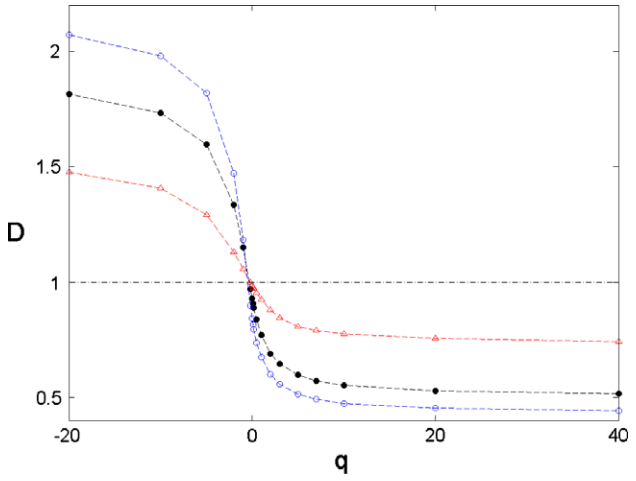

Fig. 14. Sample 3, large strain $\gamma = 56\%$; multifractal spectrum. Solid circles: all fluctuations; open circles: large fluctuations; triangles: small fluctuations.

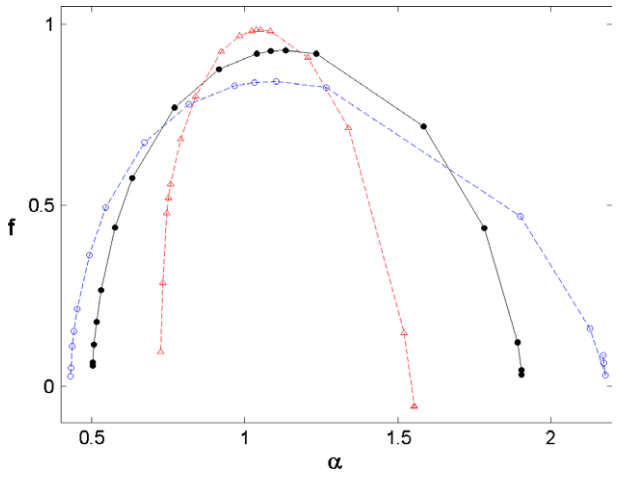

Fig. 15. Sample 3, large strain $\gamma = 56\%$; singularity spectrum. Solid circles: all fluctuations; open circles: large fluctuations; triangles: small fluctuations.

the maximum $f(\alpha)$ value is also smaller because rarefaction of the subset of fluctuations has been performed. It is also smaller than 1, which indicates some clustering of the large fluctuations along the sample axis. In contrast, the small-scale spectra (red lines) show a qualitatively different behavior: the fluctuations are less singular, and since the maximum $f(\alpha)$ value is 1, they are uniformly distributed along the axis. Therefore, conjecturing the existence of two different scaling regimes from the multifractal analysis, at small vs. large fluctuation scales, seems reasonable.

4. Interpretation

The autocorrelation function, the power spectrum density and the multifractal analysis of the dislocation density distributions suggest evolving characteristics of scale-invariance and compounded spatial correlation regimes as strain increases. Interpretation of these statistical trends is now sought through the various dislocation mechanisms involved during straining. The basal screw dislocations are primarily responsible for the accommodation of the torsion strain. They nucleate close to the edge of the sample and, driven by the applied stress, glide toward the axis, until they stop due to vanishing applied shear stress [10–12]. Their presence induces lattice distortion and elastic internal stresses, which can be taken as responsible for the long-range interaction between basal planes. Sample 1 and Fig. 4 provide an illustration for such a situation (as well as the dislocation distributions from Ref. [8]). Unlike the applied stress field, this internal stress field features non-basal (non-Schmid) components, such that glide along the prismatic planes can now be activated through cross-slip of the basal screws [10–12]. As the cross-slip distance increases the non-basal component of the internal stress field decreases, and at some point double cross-slip occurs. Edge jogs formed in prismatic planes in this process have a dual role. They both act for the multiplication of the basal screw dislocations along the c-axis and as obstacles to basal slip [11]. At this stage, relaxation of the long-range stress field tends to occur due to the distribution of basal slip along the c-axis. The organization of the dislocation distribution should therefore depend not only on the long-range stresses but also on the short-range interactions inherent to the presence of obstacles and double cross-slip [13]. At the scale where dislocation densities can be defined, cross-slip (and more extensively, any dislocation motion) is amenable to "transport" of these quantities [14,18]. To explain the observed statistical trends, we present the conjecture that the short-range interactions involved in the transport of dislocation densities are increasingly influential in the self-organization of dislocation ensembles as deformation proceeds. The conjecture is now tested by using a field dislocation model accounting for both dislocation transport and internal stresses.

The model uses the continuum description of dislocations based upon Nye's dislocation density tensor $\boldsymbol{\alpha}$ [25]. Operating on the normal $\mathbf{n}$ to a unit surface S, $\boldsymbol{\alpha}$ provides the net Burgers vector $\mathbf{b} = \boldsymbol{\alpha}.\mathbf{n}$ of all dislocations lines threading S, i.e. the incompatibility in displacement found along the Burgers circuit surrounding this surface. When surface S is so small that it is threaded by a single dislocation with Burgers vector $\mathbf{b}$ and line vector $\mathbf{t}$, $\boldsymbol{\alpha} = \mathbf{b} \otimes \mathbf{t}$ and the involved dislocation is labelled as a "geometrically necessary" or "polar" dislocation. When the size of S, i.e. the resolution length scale, is increased to the point where S is threaded by a large number of dislocations, $\mathbf{b}$ may become zero if all individual Burgers vectors compensate statistically. Then $\boldsymbol{\alpha}$ is zero, and the dislocations are unresolved and deemed "statistical". In intermediate cases, the net Burgers vector $\mathbf{b}$ is non-zero, but part of the dislocations threading S may remain unresolved. The subscripts in the density components α_{ij} then indicate respectively the net Burgers vector and line vector directions of the polar dislocations, whereas the remaining statistical dislocations are

not accounted for. Due to the incompatibility, the elastic distortion tensor $\mathbf{U_e}$ is not a gradient. It has an incompatible part, $\mathbf{U_e^\perp}$, which results from the distribution $\boldsymbol{\alpha}$ and is a solution to the incompatibility equation

$$\mathbf{curl}\ \mathbf{U_e^\perp} = \boldsymbol{\alpha} \tag{4}$$

written here at small strains. Its compatible part, $\mathbf{U_e^\parallel}$, is a gradient and $\mathbf{curl}\ \mathbf{U_e^\parallel} = 0$. Thus, it cannot be determined from Eq. (4). For small strains, $\mathbf{U_e^\parallel}$ is the difference between the displacement gradient $\mathbf{U} = \mathbf{grad}\ \mathbf{u}$ and the compatible part of the plastic distortion, $\mathbf{U_p^\parallel}$, which will be derived below. As an illustration, let us deduce from Eq. (4) the relation between the hard X-ray-measured lattice orientations and the dislocation densities in the present torsion experiments, i.e. Eq. (2). To this end, we consider applying Eq. (4) to the elastic distortion tensor $\mathbf{U_e} = \mathbf{U_e^\parallel} + \mathbf{U_e^\perp}$ and separating the symmetric and skew-symmetric parts of $\mathbf{U_e}$. Subsequent algebra leads to

$$\mathbf{grad}\ \boldsymbol{\Omega_e} = \mathbf{curl}^{\mathbf{t}}\boldsymbol{\epsilon_e} - \boldsymbol{\alpha}^{\mathbf{t}} + \frac{1}{2}tr(\boldsymbol{\alpha})\mathbf{I} \tag{5}$$

where $\boldsymbol{\Omega_e}$ is the lattice spin vector and $\boldsymbol{\epsilon_e}$ the strain tensor [26]. Assuming the contribution of the latter to the lattice spin to be negligible compared to that of dislocations (as originally assumed by Nye [25]), one gets in particular for the spin component θ_3 along the torsion axis (to be identified with θ in Eq. (2))

$$\frac{\partial\theta_3}{\partial x_3} = \frac{1}{2}(\alpha_{11} + \alpha_{22} - \alpha_{33}) \tag{6}$$

where x_3 is an indexed notation for x in Eq. (2), and $(\alpha_{11}, \alpha_{22}, \alpha_{33})$ denote respectively the screw dislocation densities along the directions $(\mathbf{e_1}, \mathbf{e_2})$ in the basal planes and $\mathbf{e_3}$ along the torsion axis. Writing $\alpha_{33} = 0$, because such screws are irrelevant for this crystal orientation, defining ρ as $\rho = (\alpha_{11} + \alpha_{22})/2b$, where b is the Burgers vector length, one retrieves Eq. (2). Hence, ρ provides the average volumetric basal screw dislocation density in terms of the lattice distortion along the torsion axis.

The stress tensor $\mathbf{T}$ is obtained from the tensor of elastic constants $\mathbf{C_e}$ as

$$\begin{aligned}\mathbf{T} &= \mathbf{C_e} : \{\mathbf{U_e}\} = \mathbf{C_e} : \{\mathbf{U_e^\parallel} + \mathbf{U_e^\perp}\} \\ &= \mathbf{C_e} : \{\mathbf{grad}\ \mathbf{u} - \mathbf{U_p^\parallel} + \mathbf{U_e^\perp}\}\end{aligned} \tag{7}$$

where $\{\mathbf{A}\}$ denotes the symmetric part of tensor $\mathbf{A}$. The part $\mathbf{T}^\perp = \mathbf{C_e} : \{\mathbf{U_e^\perp}\}$ of tensor $\mathbf{T}$ is due to the presence in the crystal of the dislocation density $\boldsymbol{\alpha}$, and the other part $\mathbf{T}^\parallel = \mathbf{C_e} : \{\mathbf{U_e^\parallel}\}$ additionally contributes to the satisfaction of the equilibrium equation

$$\mathbf{div}\ \mathbf{T} = \mathbf{0} \tag{8}$$

and of boundary conditions. At the resolution scale used in the present problem (the characteristic size of unit surface S), the total plastic distortion rate $\dot{\mathbf{U}}_\mathbf{p}$ results from the motion of the polar dislocations $\boldsymbol{\alpha}$, with (averaged over S) velocity $\mathbf{V}$, and of the statistical (mobile) dislocations through the conventional plastic velocity gradient tensor $\mathbf{L_p}$ (throughout this section, a superposed dot indicates a time derivative)

$$\dot{\mathbf{U}}_\mathbf{p} = \boldsymbol{\alpha} \times \mathbf{V} + \mathbf{L_p} \tag{9}$$

The incompatible part of $\dot{\mathbf{U}}_\mathbf{p}$, $\dot{\mathbf{U}}_\mathbf{p}\ \perp$, feeds the increment of excess dislocations through the transport equation for dislocation densities

$$\dot{\boldsymbol{\alpha}} = -\mathbf{curl}\dot{\mathbf{U}}_\mathbf{p} \tag{10}$$

whereas the compatible part, $\dot{\mathbf{U}}_\mathbf{p}^\parallel$, is used to update $\mathbf{U}_\mathbf{p}^\parallel$ in Eq. (7). Similarly, $\dot{\boldsymbol{\alpha}}$ is used to update $\boldsymbol{\alpha}$ in Eq. (4). Complemented by constitutive relations for the dislocation velocity $\mathbf{V}$ as a function of stress and dislocation orientation, and by the evolution of the statistical densities involved in the velocity gradient $\mathbf{L_p}$, Eqs. (4)–(10) form a complete set of equations, of hyperbolic character, for the evolution of stress and dislocation densities. Boundary conditions comprise the conventional stress and displacement conditions, and the specification of inward fluxes of dislocations. A more detailed account of this overarching framework can be found in Ref. [18]. It may suffice to indicate here that the theory reduces to the standard crystal plasticity framework when $\boldsymbol{\alpha}$ is the null tensor, a condition often satisfied when the scale of resolution is commensurate with the (macroscopic) sample size. In this case, long-range interactions due to lattice incompatibility are overlooked. Conversely $\mathbf{L_p} = \mathbf{0}$ when all dislocations are resolved. For computational reasons, only small-scale systems can then be solved. Owing to the macroscopic crystal size in the present problem and to the mean dislocation–dislocation distance (of order μm), a mixed approach where both $\boldsymbol{\alpha}$ and $\mathbf{L_p}$ are non-zero is appropriate [11]. Nevertheless an approximate finite-element solution is expected to be very demanding on computational resources, since an extremely high spatial resolution, of the order of the μm, is needed to account for the strong variations in the dislocation density distribution. Hence, we relinquish realistic treatment of the torsion test and choose instead a heuristic approach with a simplified model, still retaining the essential physical features, but whose finite-element approximate solution is still feasible.

By restricting the attention to screw dislocations pertaining to a single slip system in the basal plane $(\mathbf{e_1}, \mathbf{e_2})$, with Burgers vector oriented in a given direction, say $\mathbf{e_1}$, and by treating out-of-plane motion in a phenomenological way, a model for simple shear at constant velocity is derived from the above. The resulting equations are

$$\dot{U}^p_{13} = \alpha_{11}v_2 + \rho_m bv \tag{11}$$

$$\dot{\alpha}_{11} = -\dot{U}^p_{13,2} \tag{12}$$

$$T_{13,3} = 0 \tag{13}$$

$$\dot{T}_{13} = \mu(V_{1,3} - \dot{U}^p_{13}) \tag{14}$$

Here a comma indicates a partial derivative. Eq. (11) derives from Eq. (9). It describes the plastic distortion rate $\dot{U}^p_{13}$ in the glide plane as a function of the polar screw $(\alpha_{11}v_2)$ and statistical dislocation $(\rho_m bv)$ mobilities, with

the latter arising from the plastic velocity gradient $\mathbf{L_p}$. Eq. (12) is the transport equation. It stands for the nucleation of polar screw dislocations due to gradients in the plastic distortion rate. The shear stress $T_{13} = \mathbf{e_1} \cdot \mathbf{T} \cdot \mathbf{e_3}$ satisfies the equilibrium Eq. (13), where μ is again the elastic shear modulus and V_1 the material velocity in the direction $\mathbf{e_1}$. T_{13} is evolved in time according to the elastoplastic constitutive law (14). Finally, the overall boundary condition

$$\int_0^h V_{1,3} dx_3 = V \tag{15}$$

is imposed. Here, V represents a constant shear velocity gap over the height h of the sample (the imposed shear strain rate is $\dot{\gamma}_a = V/h$). Velocity-driven boundary conditions are preferred to creep in order to avoid unsteadiness in the shear rate [8,11]. Similar models were offered in the creep of ice single crystals in Refs. [11,27]. Complemented by the constitutive equations for (v, v_2, ρ_m) (to be provided below in Eqs. (18)–(20)) and initial conditions, this set of equations defines a one-dimensional boundary value problem along a radial direction in a normal cross-section of the sample. This radial direction should be no surprise, since the shear distortion rate U_{13} is accommodated by screw dislocations lying along $\mathbf{e_1}$, moving toward the center in the direction $\mathbf{e_2}$. Thus, the only space variable is x_2, to be taken in the interval $(0, R)$. Invariance along the $\mathbf{e_3}$ axis is an oversimplification of the model but, as already mentioned, out-of-basal-plane motion of dislocations will nevertheless be considered, although only through phenomenological prescriptions (see below Eq. (19)). The output of the model will consist in a dislocation distribution along a radius of the cross-section, to be compared qualitatively with the experimental dislocation distribution along the axis shown in Section 3, and of a shear stress distribution. The hope is that the features uncovered by the present experiments (the gradual pre-eminence of short-range over long-range correlations in the axis direction) are so generic that they will also show up along a radial direction in basal planes during a velocity-driven test.

Combining Eqs. (11) and (12), a generalized Burgers equation with a source term is found

$$\dot{\alpha}_{11} + (\alpha_{11} v_2)_{,2} = -(\rho_m b v)_{,2} \tag{16}$$

Such an equation is typically encountered in transport problems, most notably in fluid dynamics. Here, it serves as the equation for the transport of the screw dislocation density α_{11} along the radius. Now combining Eqs. (11) and (13–15), an evolution equation for the shear stress can be written

$$\frac{1}{\mu}\dot{T}_{13} = \dot{\gamma}_a - (\alpha_{11} v_2 + \rho_m b v) \tag{17}$$

These two partial differential equations summarize the problem. In the forthcoming calculations, strain will be limited to alleviate the need for objective derivatives of the screw density in Eq. (16) and shear stress in Eq. (17). An account of the physics of dislocation velocity and of straining history is now provided through phenomenological statements. Following Ref. [9], we assume a power-law relationship for the average polar and statistical dislocation velocities (v_2, v) in the form

$$v_2 = v\frac{\alpha_{11}}{|\alpha_{11}|}; \quad v = v_0 sgn(T_{13})\left(\frac{T_{13}}{\sigma_0 + \sigma_h}\right)^2 \tag{18}$$

Hence, the same physics applies to both dislocation species. In this simplified model, Eq. (17) provides for the spatio-temporal long-distance organization of slip activity along the sample. Internal stresses are represented by the fluctuations of T_{13} about its mean value, which is clearly a strong reduction in the complexity of the three-dimensional internal stress field. In Eq. (18), σ_h represents statistical hardening while the parameters (v_0, σ_0) are reference velocity and stress values, respectively. The latter are identified from the experimental data [9,11,28]. Isotropic statistical hardening is derived from the sessile density ρ_s in the Taylor form: $\sigma_h = \alpha\mu b\sqrt{\rho_s}$, where α is a constant. Only a fraction $(1-\beta)$ of the nucleated screws glides in the basal planes. As conjectured earlier in this section, the complementary fraction β of the nucleated screw dislocations experiences cross-slip due to non-Schmid components of stress arising from the internal stress field. Therefore the sessile density increases, due to the formation of edge segments in prismatic planes. Its rate of formation is assumed proportional to the gradient of screw mobility [11]

$$\dot{\rho}_s = \frac{\beta}{b}|(\alpha_{11} v_2)_{,2}| \tag{19}$$

Large β values reflect high probabilities of cross-slip. In all upcoming calculations, σ_h remains much smaller than the reference stress σ_0, implying that statistical hardening is relatively insignificant and that the density ρ_s of edge jogs remains limited. The mobile statistical dislocation density ρ_m has a very low initial value. It increases due to dislocation sources associated with edge jogs in prismatic planes [29]. Its nucleation rate is constant with coefficient C_1. Saturation of mobile dislocations results from their mutual annihilation, with coefficient C_2 and saturation value C_1/b^2C_2.

$$\dot{\rho}_m = \left(\frac{C_1}{b^2} - C_2\rho_m\right)|\dot{U}^p_{13}| \tag{20}$$

All material parameter values are taken from Ref. [11] and given in Table 3. Initial conditions are provided in Table 4. They are uniform in space, except for a random 0.1% node-to-node variation imposed on the initial sessile density ρ_s, the incompatible component of which will result in the nucleation of polar screws at initial time.

The main features of the numerical method we employed are now summarized. A Galerkin least-squares explicit finite-element method with linear interpolation appropriate for transport problems was used for the solution of Eq. (16) (see Ref. [30] for a detailed description of the algorithm), while a standard Galerkin method with a quadratic interpolation was used for Eq. (17). The radius R was equally divided into 30,000 elements, whose length

Table 3
Numerical constants used in the model.

b	v_0	σ_0	n	μ	R	α	β	C_1	C_2	$\dot{\gamma}_a$	h
4.5×10^{-10} m	10^{-6} m/s	1 MPa	2	3 GPa	30 mm	0.133	0.1	10^{-8}	17	10^{-6} s^{-1}	3×10^{-2} m

Table 4
Initial conditions.

ρ_m	ρ_s	α_{11}	T_{13}
10^8 m^{-2}	10^8 m^{-2}	0	0

is therefore 1 μm. This value was chosen to be less than the X-ray diffraction spatial resolution (1.7 μm) in order to avoid any measurable effect of mesh size on the analysis of the predicted distributions. Note that using such an extremely small spatial resolution over a three-dimensional sample of the same radius would result in more than 100 trillions elements, an endeavor beyond the scope of any present computing facility. In the calculations shown below, the shear strain is limited to 5% in order to keep applicability of the small strain setting.

An example of the predicted distributions is shown in Fig. 16 at 2% strain. The visual aspect is similar to the experimental distribution in Fig. 6. The multifractal analysis shown earlier was applied to the predicted distributions, with the following results. At the early stages of deformation <0.1%, the predicted distribution does not show multifractality, meaning that scale invariance is absent. Multifractality shows up for strains in the range 0.2–2%, in relation with polar dislocation mobility. The partition functions in this range are shown in Fig. 17. Two families of slopes are displayed. Straight dashed lines are visual guides for a scaling regime in the long-distance range $\delta x \sim 0.7$ mm to 11 mm. The scaling behavior is better seen, particularly for positive qs if the large fluctuations are isolated. Then the partition functions shown in Fig. 17 shift to

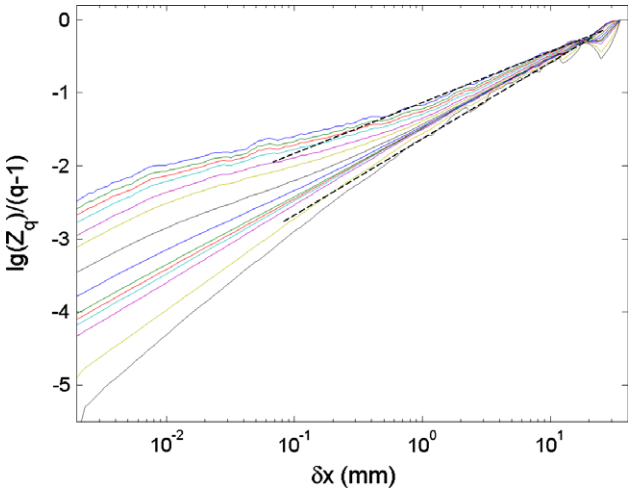

Fig. 17. Predicted partition functions, all fluctuations. Dashed lines are visual guides for the scaling interval.

those depicted in Fig. 18. The respective multifractal spectra are shown in Fig. 19. A second scaling regime takes place in the short distance range $\delta x \sim 0.01$–0.1 mm. However, the partition functions are slightly bent in this range and a smooth multifractal spectrum is not obtained. Multifractality degrades after 4% strain, and disappears at larger strains, due to increasing statistical noise. The latter reflects the mobility of statistical dislocations progressively prevailing over polar dislocation mobility. Thus the present model reproduces qualitatively the trends in the experimental results, but the correlations at small scales, although existing, are not well rendered. From the statistical point

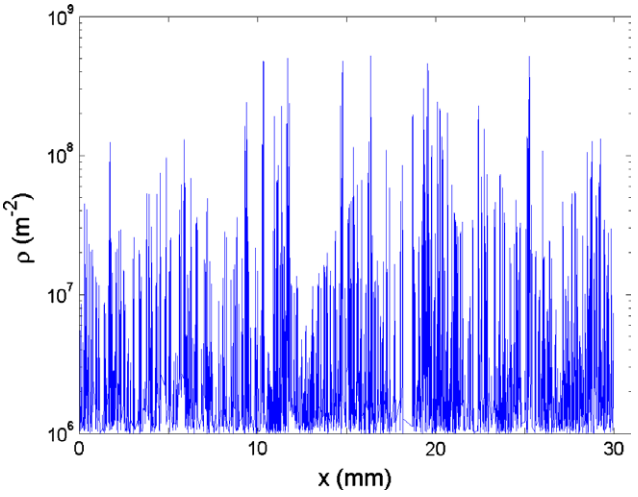

Fig. 16. Predicted polar dislocation distribution at 2% strain. Note that this is zero at initial time (see Table 4). The multifractal analysis of the fluctuations seen in this figure is shown in Figs. 17–19.

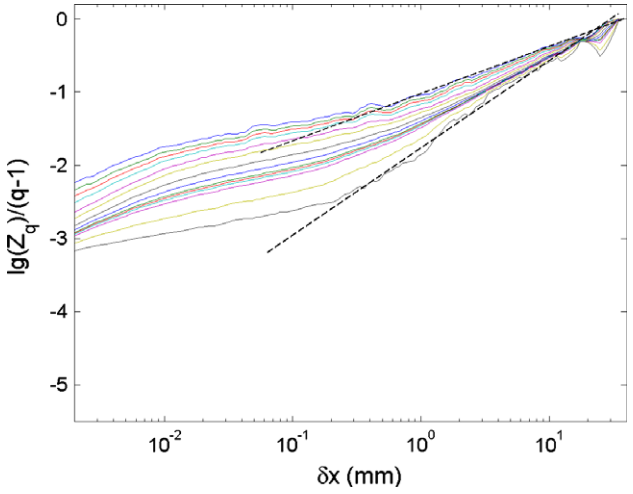

Fig. 18. Predicted partition functions, large fluctuations. Dashed lines are visuals guide for the scaling interval.

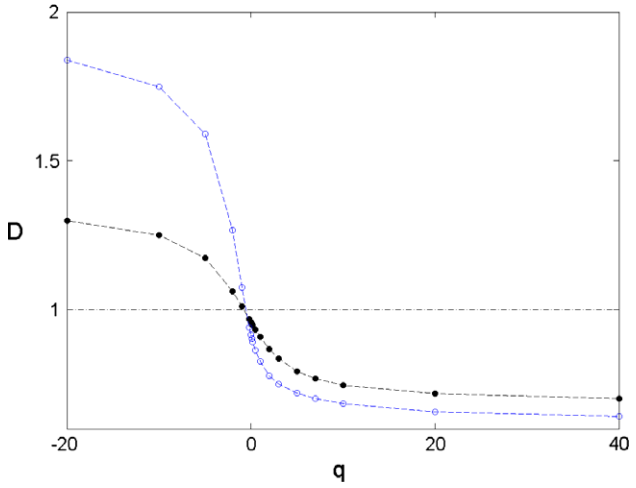

Fig. 19. Predicted multifractal spectra. Solid circles: all fluctuations, open circles: large fluctuations.

of view, two reasons can be invoked to explain such behavior: (i) the stochastic component in the predicted dislocation density distribution is too strong; and/or (ii) the intertwining of small-scale and large-scale fluctuations is too dense, which impedes efficient separation of the respective subsets of peaks in the dislocation density distributions. Both aspects might very well result from the simplifications inherent to the formulation of the one-dimensional model, which uses a phenomenological treatment for the statistical dislocations mobility and tends to underestimate the long-range interactions. Further, it is very likely that the dislocation distribution in the basal plane is less influenced by short-range interactions than along the *c*-axis. Indeed, as stress and dislocation velocity decrease in the axis area, the basal screw dislocations moving toward the axis tend to pile up in that area [10–12]. Hence, screening of the long-range correlations may not be as conspicuous along a radial direction as along the torsion axis.

5. Summary and concluding remarks

Hard X-ray diffraction provides evidence of a strongly heterogeneous distribution of dislocation densities along the axis of cylindrical ice single crystals oriented for basal slip in torsion creep. At moderate strain, the dislocation distributions display long-distance correlations with scale-invariant character [8]. However, as strain increases, a trend to decreasing autocorrelation of the dislocation distributions is observed in the autocorrelation function and Fourier power spectrum. In order to interpret such statistical behavior from the point of view of dislocation dynamics, it is conjectured that the long-range correlations seen at moderate strain reflect the lattice distortion and internal elastic stress fields associated with the basal screw dislocations accommodating torsion. Unlike the applied stress field, their long-range internal stress field presents non-basal components, which promote double cross-slip through prismatic planes. Double cross-slip plays a role in the multiplication of dislocations along the *c*-axis and in their self-organization at a short length scale. Hence, short-range correlations in relation with dislocation obstacles and cross-slip progressively screen long-range correlations when strain increases. At large strains, a multifractal analysis of the experimental dislocation density distributions confirms the existence of different scale-invariance regimes, at distinct length scales and with different scaling exponents. The mixed character (short-range vs. long-range) and the evolution of the spatial correlations in the dislocation distributions is reproduced by a heuristic model of the plasticity of single crystals based on field dislocation dynamics. This model accounts for both the long-range elastic interactions due to the presence of dislocations and the short-range interactions (dislocation obstacles, cross-slip, etc.) inherent to the transport of dislocation densities. The results suggest the pre-eminence of short-range interactions in the self-organization of dislocation ensembles at large strain, as also illustrated by recent discrete dislocation dynamics simulations in copper [15]. The continuous acceleration of creep in evidence in Fig. 1 shows, however, that the short-range interactions do not contribute as decisively to strain hardening. Indeed, statistical hardening remains very limited in ice single crystals and does not hinder creep acceleration, at least in the range of strain covered by our experiments. In contrast, multislip conditions should enhance short-range prevalence in both dislocation patterning and strain hardening in face-centered cubic crystals. Finally, our results also imply that including transport in models is essential to account for the self-organization of dislocation ensembles.

Acknowledgements

Fruitful discussions with Armand J. Beaudoin and Jérôme Weiss are gratefully acknowledged. J.C. and P.D. thank also ST2I Institute of Centre National de la Recherche Scientifique for funding support.

References

[1] Weiss J, Grasso J. J Phys Chem B 1997;101:6113–7.
[2] Miguel M, Vespignani A, Zapperi S, Weiss J, Grasso J. Nature 2001;410:667–71.
[3] Weiss J, Miguel M-C. Mater Sci Eng A 2004;387:292–6.
[4] Zaiser M. Adv Phys 2006;55(1):185–245.
[5] Dimiduk D, Woodward C, Lesar R, Uchic M. Science 2006;312:1188–90.
[6] Weiss J, Richeton T, Louchet F, Chmelík F, Dobron P, Entemeyer D, et al. Phys Rev B 2007;76:224110.
[7] Brinckman S, Kim J, Greer J. Phys Rev Lett 2008;100:155502.
[8] Montagnat M, Weiss J, Chevy J, Duval P, Brunjail H, Bastie P, et al. Philos Mag 2006;86(27):4259–70.
[9] Duval P, Ashby M, Anderman I. J Phys Chem 1983;87:4066–74.
[10] Chevy J. Viscoplasticité et hétérogénéités de déformation du monocristal de glace: expériences et simulations. PhD thesis, France: Institut polytechnique de Grenoble; 2008.

[11] Taupin V, Varadhan S, Chevy J, Fressengeas C, Beaudoin AJ, Montagnat M, et al. Phys Rev Lett 2007;99:155507.
[12] Chevy J, Montagnat M, Duval P, Fivel M, Weiss J. Dislocation patterning and deformation processes in ice single crystals deformed by torsion. In: Werner F. Kuhs, editor. Proceedings of the 11th international conference on the physics and chemistry of ice. Cambridge, UK: The Royal Society of Chemistry; 2007.
[13] Gómez-García D, Devincre B, Kubin L. Phys Rev Lett 2006;96:125503.
[14] Fressengeas C, Beaudoin A, Entemeyer D, Lebedkina T, Lebyodkin M, Taupin V. Phys Rev B 2009;79:014108.
[15] Devincre B, Hoc T, Kubin L. Science 2008;320(5884):1745–8.
[16] Lebyodkin M, Lebedkina T, Chmelík F, Lamark T, Estrin Y, Fressengeas C, et al. Phys Rev B 2009;79:174114.
[17] Lebyodkin M, Lebedkina T. Phys Rev E 2006;73:036114.
[18] Acharya A. J Mech Phys Solids 2001;49(4):761–84.
[19] Hamelin B, Bastie P. Proc SPIE 2002;4786:29–39.
[20] Ashby MF. Philos Mag 1970:21–399.
[21] Schneider J. J Appl Cryst 1974;7:547–54.
[22] Schneider J. J Appl Cryst 1974;7:541–6.
[23] Halsey T, Jensen M, Kadanoff L, Procaccia I, Shraiman B. Phys Rev A 1986;33:1141.
[24] Chhabra A, Jensen R. Phys Rev Lett 1989;62:1327.
[25] Nye J. Acta Metall 1953;1:153–62.
[26] Kröner E. Continuum theory of defects in physics of defects. In: Balian R et al., editors. Les Houches, Session XXXV, 1980. North Holland: Amsterdam; 1981.
[27] Taupin V, Richeton T, Chevy J, Fressengeas C, Weiss J, Louchet F, et al. Acta Mater 2008;56:1555–63.
[28] Shearwood C, Whitworth R. Philos Mag 1991;64:289–94.
[29] Louchet F. CR Physique 2004;5:687.
[30] Varadhan SN, Beaudoin AJ, Acharya A, Fressengeas C. Model Simulat Mater Sci Eng 2006;14:1245–70.